

Coherent control of Rydberg states in silicon

P. T. Greenland¹, S. A. Lynch¹, A. F. G. van der Meer², B. N. Murdin³, C. R. Pidgeon⁴, B. Redlich², N. Q. Vinh^{2†} & G. Aeppli¹

Laser cooling and electromagnetic traps have led to a revolution in atomic physics, yielding dramatic discoveries ranging from Bose–Einstein condensation to the quantum control of single atoms¹. Of particular interest, because they can be used in the quantum control of one atom by another, are excited Rydberg states^{2–4}, where wavefunctions are expanded from their ground-state extents of less than 0.1 nm to several nanometres and even beyond; this allows atoms far enough apart to be non-interacting in their ground states to strongly interact in their excited states. For eventual application of such states⁵, a solid-state implementation is very desirable. Here we demonstrate the coherent control of impurity wavefunctions in the most ubiquitous donor in a semiconductor, namely phosphorus-doped silicon. In our experiments, we use a free-electron laser to stimulate and observe photon echoes^{6,7}, the orbital analogue of the Hahn spin echo⁸, and Rabi oscillations familiar from magnetic resonance spectroscopy. As well as extending atomic physicists' explorations^{1–3,9} of quantum phenomena to the solid state, our work adds coherent terahertz radiation, as a particularly precise regulator of orbitals in solids, to the list of controls, such as pressure and chemical composition, already familiar to materials scientists¹⁰.

There are several approaches to atom trap physics in solids. One possibility is to use quantum dots hosted by compound semiconductors^{11,12}, which have the advantage of being addressable using conventional lasers. However, this relies on expensive fabrication and experiments have been restricted mostly to the frequency domain. Here we follow another avenue, one that requires more exotic laser technology but lends itself to straightforward time-domain measurements and has much simpler sample requirements. We use the ubiquitous semiconductor–donor combination Si:P, which opens up the possibility of exploiting sophisticated semiconductor device processing technologies for combined electrical and coherent optical control.

Our experiments make use of the remarkable fact that impurities with one more valence electron than the host semiconductor have ground and excited states corresponding to the Rydberg series of the free hydrogen atom, the touchstone for the Bohr formulation of quantum mechanics. In the semiconductor¹³, the conduction bands, with curvature characterized by the electron effective mass, m^* , play the part of the free-electron continuum, and the Coulomb interaction is reduced in proportion to its dielectric constant, ϵ_r . Thus, the binding energy scales with m^*/ϵ_r^2 and the orbital radii scale with ϵ_r/m^* . For typical donors in silicon, the lowest-energy Lyman series line is therefore in the terahertz regime: in the case of phosphorus, the $1s(A_1) \rightarrow 2p_0$ transition is at 34.2 meV, equivalent to 36.2 μm and 8.29 THz (Fig. 1a). There are also smaller level splittings associated with the broken rotational symmetry in the solid. The spatial extent of the orbitals is an order of magnitude larger than those of hydrogen in vacuum: the $2p_0$ level, for example, has an extent of ~ 10 nm,

enclosing about 10^4 silicon atoms, and is thus comparable in size to transistors already in commercial use. Previous frequency¹⁴ and time-domain studies¹⁵ have established the great longevity of the excited states, with a population lifetime, T_1 , of 200 ps for the $2p_0$ state (due to single-phonon emission augmented by intervalley and umklapp processes¹⁶) and corresponding oscillator quality factors of 2,000 or more.

A two-level atom resonantly illuminated by the high-intensity coherent light from a laser undergoes Rabi oscillations at a frequency given by $\Omega = (e\mu_{12}/\hbar)F$, where e is the charge on the electron, F is the electric field envelope of the light beam, μ_{12} is the transition dipole matrix element and \hbar is Planck's constant divided by 2π . For a pulse of finite duration, the excited-state polarization that remains in the system after the pulse has passed varies sinusoidally with the pulse area: $A = (e\mu_{12}/\hbar)F(t) dt$. If the laser is at resonance with the $1s(A_1) \rightarrow 2p_0$ transition, it will produce a linear superposition of $1s(A_1)$ and $2p_0$ wavefunctions—a very simple wave packet that oscillates in time as

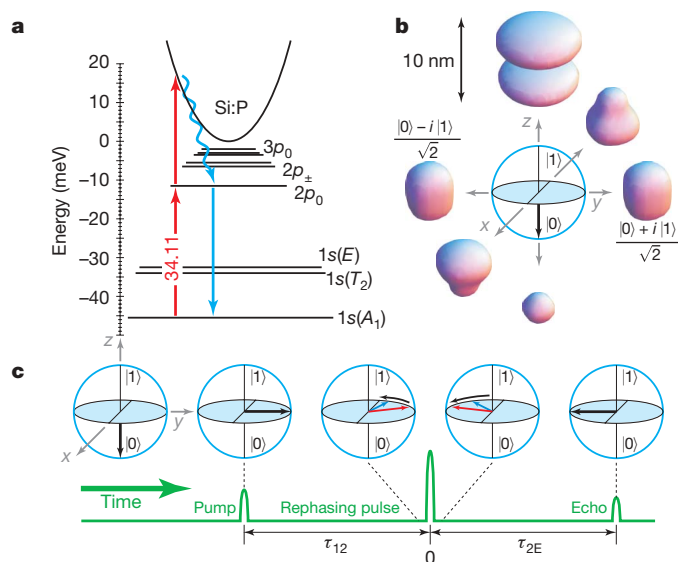


Figure 1 | The principle of the experiment. **a**, The spectrum of an isolated phosphorus donor in silicon. The primary excitation and two-photon ionization paths are shown in red; dephasing paths—photoelectron collisions and phonon decay—are shown in blue. **b**, The Bloch sphere, with some sample wave packets. The ground state, $1s(A_1)$ ($|0\rangle$), is at the south pole and the excited state, $2p_0$ ($|1\rangle$), is at the north pole. Around the equator, the wave packet varies as the relative phase of a 50:50 mixture evolves in time. This is the time-dependent combination we excite to produce the photon echo. **c**, The classic Hahn sequence, and the corresponding behaviour of the Bloch vector. Ideally, the first pulse has an area of $\pi/2$ and the second pulse has an area of π . τ_{2E} , interval between the rephasing beam and the echo.

¹London Centre for Nanotechnology and Department of Physics and Astronomy, University College London, London WC1H 0AH, UK. ²FOM Institute for Plasma Physics “Rijnhuizen”, PO Box 1207, NL-3430 BE Nieuwegein, The Netherlands. ³Advanced Technology Institute, University of Surrey, Guildford GU2 7XH, UK. ⁴Heriot-Watt University, Department of Physics, Riccarton, Edinburgh EH14 4AS, UK. †Present address: ITST, Department of Physics, University of California, Santa Barbara, California 93106-4170, USA.

the superposition precesses around the Bloch sphere (Fig. 1b), which represents the quantum mechanical state space for two-level systems.

For an ensemble, all the wave packets initially radiate in phase and therefore strongly, to produce coherent radiation. The coherence is lost, owing to small offsets in the resonant frequencies resulting from differences in the local environment, and the radiation weakens as the dipoles dephase on a timescale given by the inverse of the $1s(A_1) \rightarrow 2p_0$ inhomogeneous linewidth, which is measurable in the frequency domain using conventional continuous-wave infrared spectroscopy. However, their relative phases can be restored by a subsequent laser pulse leading to a second burst of coherent radiation, the photon echo,

which appears after a time equal to the interval between the initial and rephasing pulses, in precise analogy to the well-known Hahn spin echo (Fig. 1c). Details of the time development of the photon-echo Bloch vector, and its close analogy with the Hahn spin echo, can be found in ch. 9 of ref. 7. In general, the amplitude of the echo will decrease as a function of the time delay of the rephasing pulse, with a characteristic time T_2 , owing to population decay and stochastic phase jumps of the oscillators.

The emission appears not only at a well-defined time, but also at a well-defined angle: its direction is given by $\mathbf{k}_E = 2\mathbf{k}_2 - \mathbf{k}_1$ where \mathbf{k}_1 is the wavevector of the pump beam and \mathbf{k}_2 is that of the rephasing beam⁶.

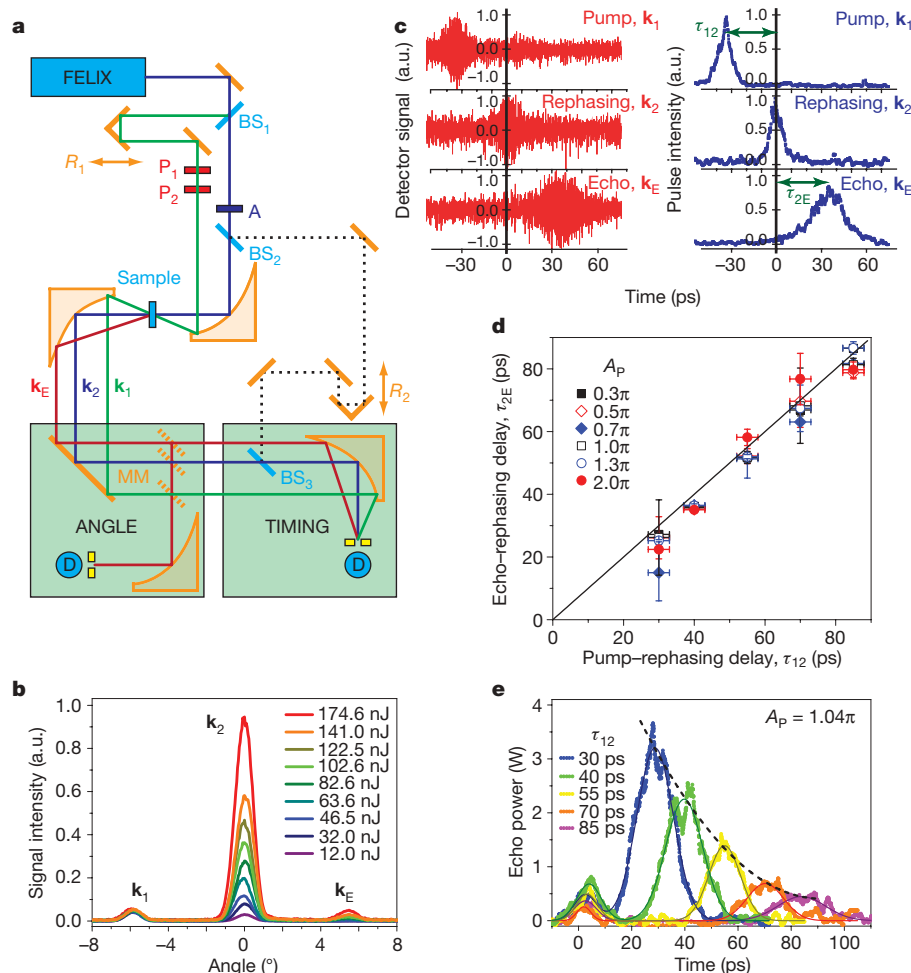


Figure 2 | Experimental orbital echo detection. **a**, Schematic of the experimental geometry. The \mathbf{k}_1 beam (green) is the pump pulse referred to in Fig. 1c and the \mathbf{k}_2 beam (blue) is the rephasing pulse in Fig. 1c. They intersect in the sample (at $\sim 5^\circ$ in the experiment) and the echo pulse (\mathbf{k}_E , red) is emitted in the direction $2\mathbf{k}_2 - \mathbf{k}_1$. The total path lengths are not drawn to scale. We show the set-up for measuring the echo direction (ANGLE) and the arrival time (TIMING), which uses cross-correlation with a reference pulse (\mathbf{k}^* , dotted line). A, attenuators; BS, beam splitter; D, detector; MM, moving mirror; P_1 , polarizer; P_2 , analyser; R, optical delay line. **b**, Angle-resolved echo. The intensities of the angle-resolved signals were recorded by translating the detector across the far field (a, ANGLE), which shows that $\mathbf{k}_E = 2\mathbf{k}_2 - \mathbf{k}_1$ as predicted. a.u., arbitrary units. **c**, Time-resolved echo. Result of cross-correlation of the reference beam (a, \mathbf{k}^* in TIMING) with the pump, the rephasing pulse and the echo by interfering them on the detector. The abscissa is the arrival time of the reference pulse relative to the arrival of the rephasing pulse. On the left is the detector signal, showing the interference patterns with the pump, rephasing and echo beams. A moving average has been subtracted to remove the background and laser drift. The pump, rephasing and echo temporal profiles were obtained from the square of these interference patterns, as shown on the right, where the pump beam/rephasing beam time interval, τ_{12} , and the rephasing beam/echo time

interval, τ_{2E} , are also shown. Gaussian fits of the pump and rephasing pulses had full-widths at half-maximum intensity of 7.7 ± 1.5 ps, consistent with the inverse spectral width, 0.28%. The echo duration, 27.8 ± 7.6 ps, is somewhat longer than would be expected from the measured inhomogeneous frequency-domain linewidth (~ 200 μ eV). **d**, Echo arrival-time control. Time-resolved cross-correlation experiments similar to those shown in **c**, with a range of pump-rephasing delays, were used to establish values of the echo delay with respect to the rephasing beam. Within the experimental error, the echo arrives when expected, that is, $\tau_{2E} = \tau_{12}$, shown by the black line. The errors in τ_{2E} are standard deviations derived from a Monte Carlo method, and the errors in τ_{12} represent the uncertainty in the pump-rephasing zero. Because the laser pulse has a Gaussian spatial profile, the effective pulse area for atoms at radius r from the pulse centre is $A(r) = A_p \exp(-r^2/2r_0^2)$, where $r_0 = 0.89$ mm and we characterize the size of the pulse by the central area, A_p (Methods). **e**, Decay of time-resolved echoes. We show a set of echo profiles for a selection of pump-rephasing delays. The ordinate is the echo power, based on an approximate calibration. The black line is a fit, with time constant $T_{\text{exp}} = 28.4$ ps, showing that the echo intensity decreases exponentially with τ_{12} , as expected. The apparent fluctuations in the echo profile are a result of the smoothing used to process the data, as in **c**.

This means that a genuine echo, as opposed to more-conventional four-wave mixing effects, where different coherent beams are present in the sample simultaneously, has signatures in space and time. To discover the orbital echo in Si:P, we accordingly set out to establish the direction of the echo beam relative to the pump and rephasing beams, the arrival time of the echo relative to the pump and rephasing pulses, and its decay as a function of rephasing pulse delay with respect to the pump pulse. All this is summarized in Fig. 2.

We performed most of our experiments on a Czochralski-grown (110) natural silicon wafer, 200 μm thick and doped with 1.5×10^{15} phosphorus donors per cubic centimetre, but also verified the key results on several other samples, as described in the Supplementary Information. The terahertz source was the FELIX free-electron laser at the FOM Institute in Nieuwegein¹⁷, which produces trains of radiation pulses that for the present experiment were tuned so that their frequency matched the $1s(A_1) \rightarrow 2p_0$ transition of Si:P and had durations of ~ 10 ps, as also verified below. We concentrated on the $2p_0$ state because of all the Rydberg states, it has the highest measured value of T_1 (ref. 15).

First, we establish the directional property of the echo ($\mathbf{k}_E = 2\mathbf{k}_2 - \mathbf{k}_1$) by measuring the angular distribution of the beams. In our experiment, the pump (\mathbf{k}_1) and rephasing (\mathbf{k}_2) beams intersect at an angle of $\sim -5^\circ$. Simple geometry shows that the echo will emerge at an angle of $\sim 5^\circ$ with respect to the direction of the rephasing beam, \mathbf{k}_2 . Figure 2b shows that this is indeed the case.

Having demonstrated the appearance of an echo signal with the correct wavevector, we turn to the verification of its arrival time, which we determine using a reference pulse split from the rephasing pulse, and a delay line. The transmitted pump, rephasing and emitted echo pulses, as well as the reference pulse, are all focused onto the detector through a pinhole to produce a characteristic interference pattern in time. The angular dispersion of the pump, rephasing and echo pulses allows us to block all but one of them in turn and separately obtain the interference pattern of each with the reference beam. By subtracting the mean intensity and squaring the result, the arrival times and shapes of the pump, rephasing and echo pulses can then be determined as functions of time (Fig. 2c). The three pulses take the form of well-defined peaks, with the maxima occurring at the times (Fig. 2d) anticipated for echoes.

We can now measure the dephasing time, T_2 , by observing the dependence of the echo intensity on the time interval, τ_{12} , between the pump and rephasing pulses¹⁸. As shown in Fig. 2e, the intensity of the echo decays exponentially, as $\exp(-\tau_{12}/T_{\text{exp}})$, and $T_2 = 4T_{\text{exp}}$, where the factor of four arises because the interval between the emission of the echo pulse and the pump pulse that caused it is twice the pump–rephasing pulse delay, and the intensity of the echo decays twice as fast as the polarization amplitude.

We find that the value of T_2 decreases as the laser intensity is increased (Supplementary Information). The extra decoherence arises because electrons produced by two-photon excitation through the $2p_0$ state of some donors can collide with the un-ionized oscillators that produce the echo, and so increase their dephasing rate. The effects of this were calculated using a two-level reduced density matrix¹⁹, including photoionization and photoelectron collisions, which is a slight extension of the more usual Bloch equations for the spin echo. We find that including these effects is sufficient to account for all the experimental observations. The value of T_2 at low laser intensity was 160 ± 20 ps.

We have demonstrated orbital echoes and long decoherence times for Si:P. To determine how well we can actually control impurity wavefunctions, that is, the extent to which we can introduce coherent superpositions of different Rydberg states, we tracked Rabi oscillations, in the standard echo detection mode, by measuring the magnitude of the echo as a function of pump pulse area. Figure 3 shows that the experimental echo intensity (purple squares in the figure) displays one complete Rabi oscillation. The experiment agrees well with the theoretical prediction (purple line), which takes into

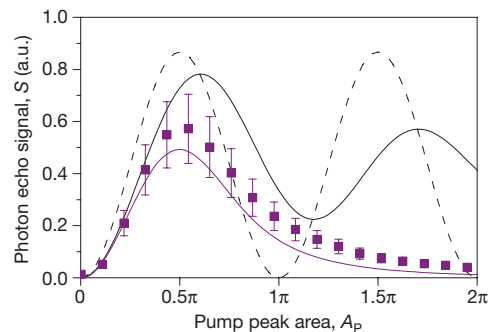


Figure 3 | Rabi oscillations. The time-integrated photon echo signal, S , as a function of pump peak pulse area, A_p , for a rephasing peak pulse area of 0.54π and a pulse length of 6.79 ps. The dashed line is the ideal theoretical result, showing Rabi oscillations. The black line shows the corrected prediction when including the non-uniform spatial profile of the laser beam, and the purple line includes the effect of both photoionization and the beam profile. The lines were calculated using values for μ_{12} , Γ_0 , σ_{2p_0} and σ_e that were found from a global fit of many experimental data sets like the one shown here. The experimental results for the same conditions are shown as points. The normalization factor for the ordinate of the experimental result relative to theory was found from a global comparison of many similar experiments with different pulse lengths and rephasing pulse areas (Supplementary Information). The error bars indicate the standard deviation of the normalization factor (systematic for an individual experiment such as the one in this figure) and dominate the statistical errors in the measurements.

account both the decoherence mechanism needed to account for the intensity dependence of T_2 and the spatial variation of intensity across the laser beam. Figure 3 also shows what would be observed if the extra decoherence and spatial intensity variations were absent.

We obtained results for several pulse durations and rephasing pulse areas (Supplementary Information). By using the theory to fit many results of this type, and by taking into account the beam attenuation due to transmission through the cryostat window, and the silicon–air interface, we calculated a dipole matrix element of $\mu_{12} = 0.28 \pm 0.03$ nm. This is much lower than the scaled hydrogenic value, as a consequence of the central-cell correction²⁰, but is comparable to values derived from low-field absorption measurements²¹, which lie in the range 0.33–0.5 nm. Because the value we determined relies on an absolute measurement of the pulse energy, which is notoriously difficult at terahertz frequencies, the agreement is satisfactory. For the photoionization cross-section from the excited state, we find $\sigma_{2p_0} = 1.28 \times 10^{-20}$ m², which is about twice what would be expected from hydrogenic scaling, and for the collision cross-section for free electrons with un-ionized donors, we obtain $\sigma_e = 8 \times 10^{-16}$ m². This is similar to electron–donor recombination cross-sections in silicon²².

We have directly observed photon echoes and Rabi oscillations produced by coherent optical excitation of phosphorus donors in silicon with intense terahertz pulses from a free-electron laser. Figure 4, which compares Si:P with an isolated hydrogen atom, summarizes the key parameters that we have deduced from our experiments. All electromagnetic parameters scale to within a factor of two of what is expected on the basis of the Bohr model with a renormalized effective mass and dielectric constant, except the $1s(A_1) \rightarrow 2p_0$ dipole matrix element, which is affected by central-cell corrections. This includes not only the Rydberg series itself but also the photoionization cross-section of the $2p_0$ state. The only substantive differences between free hydrogen and Si:P are then the much smaller T_1 and T_2 for the latter, due to phonons, which are characteristic of a solid but not of the vacuum.

Our work shows that we can prepare coherent mixtures of different orbital states for one of the most common impurities in the most common semiconductor. These mixtures have dephasing times in excess of 100 ps, which is three orders of magnitude larger than the 100 fs corresponding to the frequency of the transition between the

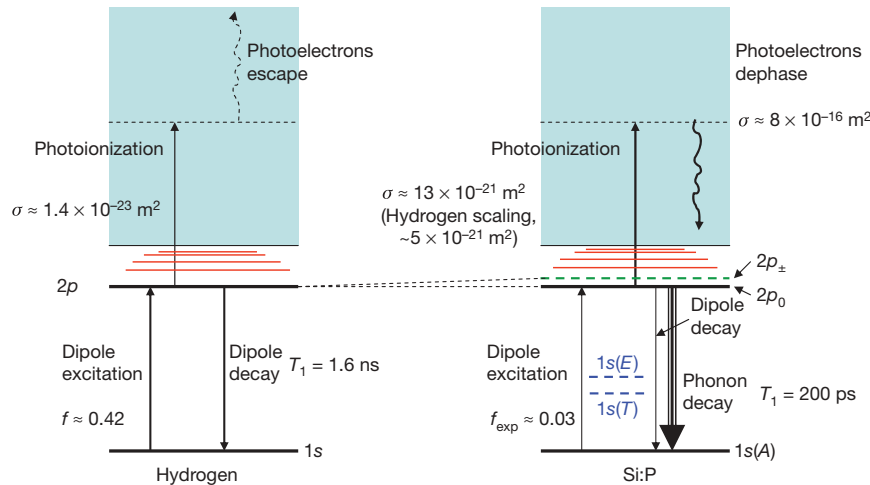


Figure 4 | Comparison of hydrogen and Si:P, showing spectra and the principal excitation and decoherence mechanisms. The crystal environment leads to an asymmetric effective mass, so that the hydrogen $2p$ state splits into $2p_0$ and $2p_{\pm}$ states in Si:P. Additionally, the crystal field further splits the hydrogen-like levels into states of cubic symmetry; the splitting of the $1s$ level into its A , T and E components is shown, but the splitting in the excited states is too small to display here. The main decay

orbital states. The frequency-domain homogeneous linewidth associated with our measured T_2 value, 160 ps, is $8.2 \mu\text{eV}$. The inhomogeneous linewidth reported for phosphorus in isotopically pure float-zone silicon is about half of this¹⁴, which implies that in isotopically pure silicon T_2 must be greater than ~ 320 ps, so there is reason to believe that more carefully prepared samples will have longer dephasing times than the Czochralski-grown silicon used here.

Coherent control of donor orbitals in silicon opens up many possibilities under examination at present using atom traps^{1–3}, such as entanglement of pairs of impurities whose ground-state wavefunctions are too compact to interact. The pulses used in the experiments described above can be used to coherently control arbitrarily small numbers of impurities, such as those positioned deterministically in silicon by means of scanning probe nanolithography²³. The exploitation of coherent effects in single impurities will depend on the development of electrical techniques for read-out²⁴, and this is likely to be easier in silicon-based structures than in alternatives. Such technologies will, for example, allow the coherent control of impurities to be used for the regulation of magnetism⁵ by opening and closing exchange pathways through the timed preparation of excited states.

METHODS SUMMARY

Figure 2a is a schematic of our experiment. The laser source was a free-electron laser which provides terahertz pulses that are tunable, intense ($\sim 1 \mu\text{J}$), short (~ 10 ps), coherent and bandwidth limited. We used pellicle beam splitters to produce the pump, rephasing and reference pulses, which were independently delayed by controlling their optical path lengths. The pulse energies were controlled using either a set of calibrated wire-grid attenuators or a polarizer–analyser pair. The polarization on the sample was always linear. Beams were focused using a parabolic mirror onto the sample, which was held at a temperature of 4 K using a helium cryostat. The sample was $200 \mu\text{m}$ thick Czochralski-grown silicon with a phosphorus density of $1.5 \times 10^{15} \text{ cm}^{-3}$. The $1s(A_1) \rightarrow 2p_0$ transition had a full-width at half-maximum of $200 \mu\text{eV}$ as determined by Fourier transform infrared spectroscopy. Emerging beams were collimated and refocused on a helium-cooled Ge:Ga detector. Arrival-time information was achieved by interfering different pulses with a reference (that is, linear cross-correlation). The resulting interference signal had a moving average removed and was then squared and smoothed to produce the cross-correlation power trace.

To describe our experimental results, we solved a two-level density matrix ρ parametrized by $\gamma = 1/T_1$, the population decay rate; Δ , the detuning of the laser from the atomic line centre; and $\Omega(t) = eF(t)\mu_{12}/\hbar$, the instantaneous Rabi frequency. The population loss was augmented by $\gamma' = \sigma_{2p_0} I(t)/\epsilon$, the rate of photoionization from level two, where $I(t)$ is the laser intensity profile and ϵ is the

channel of the $2p_0$ state in Si:P, unlike in hydrogen, is phonon decay; furthermore, photoionization of this state is also relatively much stronger than in hydrogen, and because the photoelectrons are confined to the conduction band they can cause decoherence through phase-changing collisions. σ , cross-section of photoionization from upper state or dephasing, as labelled; f , transition oscillator strength in hydrogen; f_{exp} , measured transition oscillator strength in Si:P.

photon energy. For $\gamma' = 0$, the problem reduces to that of solving the usual Bloch equations. The decoherence rate is $1/T_2 = \Gamma = \Gamma_0 + n_e v_e \sigma_e$, where $n_e = n_0 p_e$ is the photoelectron density, n_0 is the donor density, $p_e = 1 - \rho_{11} - \rho_{22}$ is the electron ionization probability, Γ_0 is the intrinsic off-diagonal rate, v_e is the mean photoelectron velocity (which we take to be given by the kinetic energy after photoionization) and σ_e the electron–donor scattering cross-section. Solution thus requires values for μ_{12} , σ_{2p_0} , Γ_0 and σ_e (T_1 and n_0 were experimentally measured or taken from the literature).

Full Methods and any associated references are available in the online version of the paper at www.nature.com/nature.

Received 9 November 2009; accepted 20 April 2010.

1. Haeflner, H., Roos, C. F. & Blatt, R. Quantum computing with trapped ions. *Phys. Rep.* **469**, 155–203 (2008).
2. Urban, E. *et al.* Observation of Rydberg blockade between two atoms. *Nature Phys.* **5**, 110–113 (2009).
3. Gaëtan, A. *et al.* Observation of collective excitation of two individual atoms in the Rydberg blockade regime. *Nature Phys.* **5**, 115–118 (2009).
4. Schwarzschild, B. Experiments show blocking interaction of Rydberg atoms over long distances. *Phys. Today* **62**, 15–18 (2009).
5. Stoneham, A. M., Fisher, A. J. & Greenland, P. T. Optically driven silicon-based quantum gates with potential for high-temperature operation. *J. Phys. Condens. Matter* **15**, L447–L451 (2003).
6. Abella, I. D., Kurnit, N. A. & Hartmann, S. R. Photon echoes. *Phys. Rev.* **141**, 391–405 (1966).
7. Allen, L. & Eberly, J. H. *Optical Resonance and Two-level Atoms* 195–220 (Dover, 1987).
8. Hahn, E. L. Spin echoes. *Phys. Rev.* **80**, 580–594 (1950).
9. Raitzsch, U. *et al.* Echo experiments in a strongly interacting Rydberg gas. *Phys. Rev. Lett.* **100**, 013002 (2008).
10. Tokura, Y. & Nagaosa, N. Orbital physics in transition-metal oxides. *Science* **288**, 462–468 (2000).
11. Zrenner, A. *et al.* Coherent properties of a two-level system based on a quantum dot photodiode. *Nature* **418**, 612–614 (2002).
12. Kroner, M. *et al.* Rabi splitting and ac-Stark shift of a charged exciton. *Appl. Phys. Lett.* **92**, 031108 (2008).
13. Kohn, W. & Luttinger, J. M. Theory of donor states in silicon. *Phys. Rev.* **98**, 915–922 (1955).
14. Karaiskaj, D., Stotz, J. A. H., Meyer, T., Thewalt, M. L. W. & Cardona, M. Impurity absorption spectroscopy in ^{28}Si : the importance of inhomogeneous isotope broadening. *Phys. Rev. Lett.* **90**, 186402 (2003).
15. Vinh, N. Q. *et al.* Silicon as a model ion trap: time domain measurements of donor Rydberg states. *Proc. Natl Acad. Sci. USA* **105**, 10649–10653 (2008).
16. Tsyplenkov, V. V., Demidov, E. V., Kovalevski, K. A. & Shastin, V. N. Relaxation of excited donor states in silicon with emission of intervalley phonons. *Semiconductors* **42**, 1016–1022 (2007).
17. Oepets, D. van der Meer, A. F. G. & van Amersfoort, P. W. The free electron laser facility FELIX. *Infrared Phys. Technol.* **36**, 297–308 (1995).

18. Shoemaker, R. L. in *Laser and Coherence Spectroscopy* (ed. Steinfeld, J. I.) 197–372 (Plenum, 1978).
19. Agarwal, G. S. Quantum statistical theory of optical resonance phenomena in fluctuating laser fields. *Phys. Rev. A* **18**, 1490–1506 (1978).
20. Larsen, D. M. Concentration broadening of absorption lines from shallow donors in multivalley bulk semiconductors. *Phys. Rev. B* **67**, 165204 (2003).
21. Jagannath, C., Grabowski, Z. W. & Ramdas, A. K. Linewidths of the electronic excitation spectra of donors in silicon. *Phys. Rev. B* **23**, 2082–2098 (1981).
22. Brown, R. A. & Rodriguez, S. Low-temperature recombination of electrons and donors in n-type germanium and silicon. *Phys. Rev.* **153**, 890–900 (1967).
23. Ruess, F. J. *et al.* Towards atomic-scale device fabrication in silicon using scanning probe microscopy. *Nano Lett.* **4**, 1969–1973 (2004).
24. Petta, J. R. *et al.* Coherent manipulation of electron spins in semiconductor quantum dots. *Science* **309**, 2180–2184 (2005).

Supplementary Information is linked to the online version of the paper at www.nature.com/nature.

Acknowledgements We are grateful for conversations with A. J. Fisher, A. M. Stoneham, C. Kay and G. Morley; to R. Hulet for pointing out ref. 8; and for experimental assistance from K. Litvinenko and G. Morley. We acknowledge financial support from the Netherlands Organisation for Scientific Research and the Engineering and Physical Sciences Research Council (COMPASSS, grant reference EP/H026622/1, and Advanced Research Fellowship EP/E061265/1).

Author Contributions N.Q.V. and C.R.P. initiated this work; P.T.G., S.A.L., B.N.M., N.Q.V. and G.A. designed the research programme; N.Q.V., P.T.G., S.A.L., A.F.G.v.d.M. and B.R. performed the experiments; P.T.G. performed the theory and analysis; and P.T.G., B.N.M., S.A.L. and G.A. wrote the paper.

Author Information Reprints and permissions information is available at www.nature.com/reprints. The authors declare no competing financial interests. Readers are welcome to comment on the online version of this article at www.nature.com/nature. Correspondence and requests for materials should be addressed to P.T.G. (ptg@globalnet.co.uk).

METHODS

Experimental procedure. Figure 2a is a schematic of our experiment. We performed coherent optical excitation experiments in the high-field limit on the bound orbital states of phosphorus donors in commercially available silicon samples. This required tunable, short, intense, coherent terahertz pulses, which we obtained using the free-electron laser FELIX in Nieuwegein¹⁷. The laser pulses had a duration of ~ 10 ps (controllable by detuning the synchronization between the electron pulses from the accelerator and the laser cavity length), and this laser has previously been shown to be bandwidth limited using cross-correlation with a femtosecond pulsed visible laser²⁵. The pulses were separated by 40 ns and arrived in a ~ 5 - μ s bursts, called ‘macropulses’, with a 5-Hz repetition rate.

To perform the time-integrated echo experiments (Figs 2b and 3), we split the laser into two beams—the pump (\mathbf{k}_1) and rephasing (\mathbf{k}_2) beams—using a polypropylene pellicle beam splitter (BS₁). The reflected beam, \mathbf{k}_1 , travelled down an optical path with controllable length (R_1) to provide a variable delay. The \mathbf{k}_1 beam emerged from the analyser parallel to, but spatially separated from, \mathbf{k}_2 . The spatially separated beams were reflected from a large, gold-coated, off-axis parabolic mirror to a focus on the sample, which was held in vacuum on the cold finger of a helium flow cryostat with polypropylene-film windows. The focused laser spot size was measured (by focusing through a variety of fixed-diameter pinholes) to be 0.89 mm (Gaussian radius parameter). The angular separation of the beams at the sample was $\sim 5^\circ$. The emerging pump and rephasing beams, and the echo beam (\mathbf{k}_E), were collected on a second off-axis parabolic mirror and collimated before refocusing on the detector.

To minimize the effects of water-vapour absorption in the atmosphere, all beams were transported in vacuum or a dry-nitrogen-filled tank until just before the focusing mirror. The focusing mirror, cryostat and detector were in a dry-nitrogen-purged tent, with paths of ~ 40 cm in front of and behind the sample.

The pulses have energies of up to ~ 1 μ J, as measured using a calibrated pyroelectric power meter. The intensity of the beams could be controlled either by a set of calibrated wire-grid attenuators (A) or by a variable attenuator consisting of a motorized polarizer (P₁) and a fixed analyser (P₂). The electric field polarization of the laser was always linear.

For the angle-resolved echo experiment (Fig. 2b), a small mirror oriented at 45° to the beam was translated across the far field to reflect the different beams behind the sample (as shown in Fig. 2a, ANGLE). To collect the data in Fig. 2b, we set the delay in the arrival time of the rephasing pulse relative to the pump to a small, positive value, ~ 20 ps. A range of different rephasing pulse energies are shown; the pump energy was fixed.

For the time-integrated echo experiments, in which we measured the intensity dependence shown in Fig. 3, the far-field mirror was fixed and the intensity of the pump beam was varied at fixed rephasing beam intensity. Similar time-integrated experiments (Supplementary Information) were performed in which we varied the intensity of both beams in a fixed ratio and varied the time delay between the pump and rephasing beams at fixed intensities.

For the time-resolved echo experiments (Figs 2c–e), each of the exit beams (\mathbf{k}_1 , \mathbf{k}_2 and \mathbf{k}_E) were made to interfere with a fourth, reference, pulse (\mathbf{k}^*) derived from a small portion of \mathbf{k}_2 (as shown in Fig. 2a, TIMING). The reference pulse was sent through a second optical delay line (of length R_2) and then it and the exit beams were focused through a 0.4-mm-diameter pinhole at the detector. Pairwise combinations of the three exit beams were blocked to produce the linear cross-correlation of the reference with each in turn, as shown in Fig. 2c. The interference signal had a moving average removed and was then squared and smoothed to produce the cross-correlation power traces shown in Fig. 2c (right) and Fig. 2e. The centre of the echo cross-correlation was used to find the echo arrival time (Fig. 2d), and the decay of its peak as a function of time delay was used to find the homogeneous coherence lifetime (Fig. 2e).

In all experiments the detector used was a liquid-helium-cooled Ge:Ga detector, whose response time was much greater than 40 ns. The measured signals were therefore all averaged over the macropulse burst and further boxcar-averaged over several (usually five) macropulses. In all cases described above, scans (of delay, intensity and so on) were repeated and averaged.

The data presented were obtained using a 200- μ m-thick Czochralski-grown silicon sample with a phosphorus doping density of 1.5×10^{15} cm⁻³, but we also

observed echoes (not shown) in other Czochralski-grown samples and in float-zone samples of broadly similar specification. The sample was characterized using continuous-wave Fourier transform infrared spectroscopy, and the $1s(A_1) \rightarrow 2p_0$ transition was found to have a width of 200 μ eV.

Theoretical model. To describe our experimental results, we used a theoretical model that augments the standard echo theory with an extra source of decoherence due to photoionization. The two-level reduced density matrix, $\rho(t)$, which represents a slight extension of the more usual Bloch equations, is given by

$$\begin{pmatrix} \dot{\rho}_{12} \\ \dot{\rho}_{21} \\ \dot{\rho}_{11} \\ \dot{\rho}_{22} \end{pmatrix} = \begin{pmatrix} -\Gamma + i\Delta & 0 & i\Omega/2 & -i\Omega/2 \\ 0 & -\Gamma - i\Delta & -i\Omega/2 & i\Omega/2 \\ i\Omega/2 & -i\Omega/2 & 0 & \gamma \\ -i\Omega/2 & i\Omega/2 & 0 & -\gamma - \gamma' \end{pmatrix} \begin{pmatrix} \rho_{12} \\ \rho_{21} \\ \rho_{11} \\ \rho_{22} \end{pmatrix}$$

where a dot denotes a time derivative, $\gamma = 1/T_1$ is the rate at which the excited-state population decays to the ground state and $\Gamma = 1/T_2$ is the decoherence rate. The instantaneous laser coupling is given by $\Omega/2$ with $\Omega(t) = eF(t)\mu_{12}/\hbar$, where F is the (time-dependent) electric field envelope due to the laser and μ_{12} is the $1s(A_1) \rightarrow 2p_0$ dipole moment; $\Omega(t)$ is thus the instantaneous Rabi frequency. Because it reflects the echo pulse sequence, Ω is a function of time, but we have not explicitly indicated this. Finally, Δ is the detuning of the laser from the atomic line centre and γ' is the rate of irreversible population loss from the upper level.

For $\gamma' = 0$, we have the usual Bloch equations, but we relate γ' to the photoionization rate from the upper level, implying that $\gamma' = \sigma_{2p_0} I(t)/\varepsilon$, where σ_{2p_0} is the photoionization cross-section from the excited state, $I(t)$ is the laser intensity at time t and ε is the photon energy (such that $I(t)/\varepsilon$ is the photon flux). The photoelectrons thus produced also represent a source of decoherence that adds to the off-diagonal decay rate, Γ , such that

$$\Gamma = \Gamma_0 + n_e v_e \sigma_e = \Gamma_0 + n_0 p_e v_e \sigma_e$$

for a photoelectron density of $n_e = n_0 p_e$, where n_0 is the donor density and $p_e = 1 - \rho_{11} - \rho_{22}$ is the electron ionization probability. Here Γ_0 is the intrinsic off-diagonal decay rate, v_e is the mean photoelectron velocity and σ_e is the electron-donor scattering cross-section. This leads to an intensity-dependent echo decay rate. We note that the correction to Γ_0 is proportional to n_0 . This means that for lower donor densities, there is less intensity-dependent dephasing. However, the echo signal is proportional to n_0^2 (ref. 18), so although reducing the donor density has a beneficial effect on the decoherence, it also drastically reduces the echo signal.

Finally, to compare with experiment we must average over the spatial distribution of the FELIX beam. The instantaneous laser intensity envelope at time t and radial distance r from the pulse centre may be written

$$I(r, t) = I_p \exp(-r^2/r_0^2) \exp(-t^2/t_0^2)$$

where, in our experiments, $r_0 = 0.89$ mm and $t_0 \approx 10$ ps. Integrating over all space and time gives E , the total pulse energy, in terms of the peak power, I_p : $E = \pi^{3/2} r_0^2 t_0 I_p$. The laser field at r is

$$F(r, t) = F_p \exp(-r^2/2r_0^2) \exp(-t^2/2t_0^2)$$

where the peak field is given by $F_p = \sqrt{2I_0/\varepsilon_0 c}$. Atoms at r will therefore see a pulse area of

$$A(r) = \frac{e\mu_{12}}{\hbar} \int F(r, t) dt = A_p \exp(-r^2/2r_0^2)$$

with peak value $A_p = t_0 \sqrt{4\pi I_p/\varepsilon_0}$.

To model the experimental measurement, we calculated the radially averaged signal, defined as $S(A_p) = 2\pi \int r s[A(r)] dr$, where $s[A(r)]$ is the signal from atoms at radius r .

25. Knippels, G. M. H. *et al.* Generation and complete electric-field characterization of intense ultrashort tunable far-infrared laser pulses. *Phys. Rev. Lett.* **83**, 1578–1581 (1999).